

# Outflows from accretion disks formed in neutron star mergers: effect of black hole spin

Rodrigo Fernández<sup>1,2</sup>, Daniel Kasen<sup>1,3</sup>, Brian D. Metzger<sup>4</sup>, Eliot Quataert<sup>2</sup>

<sup>1</sup> *Department of Physics, University of California, Berkeley, CA 94720, USA.*

<sup>2</sup> *Department of Astronomy & Theoretical Astrophysics Center, University of California, Berkeley, CA 94720, USA.*

<sup>3</sup> *Nuclear Science Division, Lawrence Berkeley National Laboratory, Berkeley, CA 94720, USA.*

<sup>4</sup> *Columbia Astrophysics Laboratory, Columbia University, New York, NY 10027, USA.*

Submitted to MNRAS

## ABSTRACT

The accretion disk that forms after a neutron star merger is a source of neutron-rich ejecta. The ejected material contributes to a radioactively-powered electromagnetic transient, with properties that depend sensitively on the composition of the outflow. Here we investigate how the spin of the black hole remnant influences mass ejection on the thermal and viscous timescales. We carry out two-dimensional, time-dependent hydrodynamic simulations of merger remnant accretion disks including viscous angular momentum transport and approximate neutrino self-irradiation. The gravity of the spinning black hole is included via a pseudo-Newtonian potential. We find that a disk around a spinning black hole ejects more mass, up to a factor of several, relative to the non-spinning case. The enhanced mass loss is due to energy release by accretion occurring deeper in the gravitational potential, raising the disk temperature and hence the rate of viscous heating in regions where neutrino cooling is ineffective. The mean electron fraction of the outflow increases moderately with BH spin due to a highly-irradiated (though not neutrino-driven) wind component. While the bulk of the ejecta is still very neutron-rich, thus generating heavy  $r$ -process elements, the leading edge of the wind contains a small amount of Lanthanide-free material. This component can give rise to a  $\lesssim 1$  day blue optical ‘bump’ in a kilonova light curve, even in the case of prompt BH formation, which may facilitate its detection.

**Key words:** accretion, accretion disks — dense matter — gravitational waves — hydrodynamics — neutrinos — nuclear reactions, nucleosynthesis, abundances

## 1 INTRODUCTION

Binary neutron star (NS) and neutron star – black hole (BH) mergers are prime candidates for detection of gravitational waves (GW) with upcoming ground-based interferometers such as Advanced LIGO, Virgo, and KAGRA (e.g., Abadie et al. 2010). Material ejected in these mergers is expected to generate an electromagnetic (EM) counterpart powered by the radioactive decay of elements synthesized during the expansion (Li & Paczyński 1998; Metzger et al. 2010; Roberts et al. 2011; Grossman et al. 2014). Good knowledge of the properties of these EM counterparts would help with planning follow-up searches of GW sources (e.g., Bloom et al. 2009; Metzger & Berger 2012; Nissanke et al. 2013; Ghosh & Nelemans 2014; Kasliwal & Nissanke 2014; Singer et al. 2014).

The nature of the EM counterpart depends crucially on the optical opacity of the ejected material, which is sensitive to composition. In particular, very neutron-rich material (with electron fractions  $Y_e \lesssim 0.2$ ) produces heavy

$r$ -process elements upon decompression, a prediction that allows these sources to be a leading candidate for the  $r$ -process site (Lattimer & Schramm 1974; Freiburghaus et al. 1999; Korobkin et al. 2012; Goriely et al. 2013). The presence of elements with mass number  $A > 140$  is also accompanied by a dramatic increase in the optical opacity relative to iron-peak matter (Kasen et al. 2013). The resulting EM supernova-like counterpart peaks in the near infrared (IR) band on a timescale of  $\sim$  weeks (Barnes & Kasen 2013; Tanaka & Hotokezaka 2013). Such an  $r$ -process *kilonova* may have already been detected in the afterglow of GRB 130603B (Tanvir et al. 2013; Berger et al. 2013).

Mergers can eject material via three mechanisms. First, tidal forces lead to the expulsion of matter on the dynamical time (e.g., Korobkin et al. 2012; Bauswein et al. 2013; Hotokezaka et al. 2013; Foucart et al. 2014). The amount of material ejected depends on the mass ratio and the spin of both components, although in most cases this *dynamical ejecta* is very neutron-rich ( $Y_e \lesssim 0.1$ ), has

high velocities ( $\sim 0.1 - 0.3c$ ), and is confined mostly to the orbital plane. Second, neutrino irradiation of the remnant accretion disk can lead to a thermally-driven wind (e.g., McLaughlin & Surman 2005; Surman et al. 2006, 2008; Wanaajo & Janka 2012). Whether this mechanism leads to any mass ejection is highly dependent on the level of neutrino irradiation, becoming most important when a hypermassive neutron star (HMNS) phase precedes BH formation (e.g., Dessart et al. 2009; Metzger & Fernández 2014; Perego et al. 2014). This outflow is generally driven toward polar regions, carrying a higher proton content than the dynamical ejecta ( $Y_e \sim 0.3 - 0.4$ ).

Third, outflows are driven on longer timescales by a combination of angular momentum transport, nuclear recombination, and the decrease in neutrino emission as the disk temperature falls (Metzger et al. 2009; Lee et al. 2009). When the central object is a promptly-formed, non-spinning BH, this mechanism can eject several percent of the initial disk mass in a neutron-rich and quasi-spherical outflow (Fernández & Metzger 2013a, hereafter FM13). A long-lived HMNS leads to significantly larger mass ejection, with higher mean electron fraction ( $Y_e \sim 0.3 - 0.4$ ). Recently, Just et al. (2014) have examined this mass ejection mechanism including the effect of BH spin and employing energy-dependent neutrino transport, finding that a larger fraction of the initial disk mass ( $\sim 20\%$ ) is ejected, with higher electron fractions ( $Y_e \sim 0.3$ ), relative to the non-spinning case studied by FM13 and Metzger & Fernández (2014).

Numerical simulations of NS-NS mergers find remnant black hole spins in the range  $a = 0.7 - 0.9$ , with the exact value depending on the mass ratio of the binary, the spin of each component, the equation of state, and the numerical resolution (Oechslin et al. 2007; Kiuchi et al. 2009; Rezzolla et al. 2010). In addition, general relativistic magnetohydrodynamic simulations of radiatively-inefficient accretion disks around BHs find that the magnitude of the energy and mass ejection in the non-relativistic wind depend on the spin of the BH (McKinney et al. 2012; Sądowski et al. 2013).

The goal of this paper is to systematically study the effect of the gravitational potential of a spinning BH on the magnitude and composition of the outflows from remnant accretion disks. To this end, we extend the approach of FM13 and Metzger & Fernández (2014) to include a pseudo-Newtonian potential that models the spacetime of a spinning BH. We employ two different prescriptions for neutrino irradiation in order to separate differences in the results due to gravity and weak interactions. While we do not include general relativity in our simulations, the effects of a smaller innermost stable orbit on the outflow obtained with a pseudo-Newtonian potential should persist when adding more detailed physics, since basic considerations dictate that more energy is released around a spinning BH.

The structure of this paper is the following. Section 2 summarizes the numerical implementation, discusses the properties of the pseudo-Newtonian potential, and describes the list of models evolved. Results are presented in §3, separated into dynamics and composition of the outflow. Our main conclusions are summarized in §4, where we also discuss implications for EM counterparts of GW sources, and the production of  $r$ -process elements.

## 2 METHODS

### 2.1 Equations, Microphysics, and Numerical Approach

We solve the compressible hydrodynamic equations using FLASH3.2 (Dubey et al. 2009). The public version of the code has been modified to include a non-uniform grid (Fernández 2012) and source terms to model the long-term evolution of compact object merger remnant accretion disks (FM13; Fernández & Metzger 2013b; Metzger & Fernández 2014). The equation of state is that of Timmes & Swesty (2000), with abundances of neutrons, protons and alpha particles satisfying nuclear statistical equilibrium (NSE) above a temperature of  $5 \times 10^9$  K, and accounting for the nuclear binding energy of alpha particles.

Angular momentum transport is mediated by an anomalous shear stress tensor, using the kinematic viscosity of Shakura & Sunyaev (1973). The gravity of the BH is modeled by a pseudo-Newtonian potential (§2.2), ignoring the contribution from the disk.

Neutrino source terms are modeled in two ways. The first implementation is that of FM13, which includes a geometric self-irradiation prescription that applies finite optical depth corrections to otherwise optically thin emissivities. This method is suitable for disks that are at most marginally optically thick to neutrinos. The second approach is a neutrino leakage scheme (Metzger & Fernández 2014) based on the method of Ruffert et al. (1997). In both cases, the evolution of the electron fraction and the net energy deposition are followed self-consistently. Only charged-current weak interactions are included.

The computational domain is discretized in spherical polar coordinates, with a radial grid logarithmically spaced and an angular grid equispaced in  $\cos\theta$ , covering the interval  $\theta \in [0, \pi]$ . The inner radial boundary is placed midway between the innermost stable circular orbit (ISCO) and the horizon radius. The outer radial boundary is located at a radius  $10^3$  times larger. A total of 192 cells in radius and 56 in angle are used, corresponding to  $\Delta r/r \simeq \Delta\theta \simeq 2^\circ$  at the equator. One model is evolved at double resolution in angle and radius to verify convergence. The boundary conditions are reflecting in angle, and outflow in radius.

The initial condition is an equilibrium torus constructed with the Helmholtz EOS, nuclear abundances in NSE, the pseudo-Newtonian potential of §2.2, as well as constant angular momentum, entropy, and electron fraction. As in FM13 and Metzger & Fernández (2014), the torus is allowed to relax for 100 orbits (measured at the initial density peak) without neutrino or viscous source terms, in order to separate initial transients from genuine disk winds. After this time, the radial velocity is reset and source terms are turned on. We set a density floor at  $1 \text{ g cm}^{-3}$  and a cutoff density for source terms at  $10 \text{ g cm}^{-3}$  to avoid numerical problems near the inner boundary. In the case of the models with leakage scheme, this floor has a radial variation  $\propto r^{-3}$ , starting at values 10 times higher than the fiducial constant values at the inner boundary.

### 2.2 Gravity of a Spinning BH

We account for the gravity of a spinning BH through the pseudo-Newtonian potential of Artemova et al. (1996).

**Table 1.** List of evolved models and summary of results. The first five columns show model name, BH spin parameter, ISCO radius (in units of  $r_g = GM_{\text{bh}}/c^2$ ), initial torus mass, and type of neutrino treatment (Leak: leakage scheme, Thin: optically-thin with corrections), respectively. The following six columns show integrated properties of the outflow, restricted to equatorial ( $\theta \in [30^\circ, 150^\circ]$ ) and polar ( $\theta < 30^\circ$  and  $\theta > 150^\circ$ ) latitudes. The three columns in each group show the mass-flux weighted (eq. 7) electron fraction, entropy, and expansion time at a radius where the mass-flux weighted temperature is  $5 \times 10^9$  K, respectively. The 12th column shows the ratio of polar to equatorial mass ejection at the radius where the polar outflow is measured, when present. The last two columns show the mass ejection at all angles, total and unbound, at a radius of  $\sim 10^9$  cm in units of the initial torus mass.

Model	$a$	$r_{\text{ISCO}}$ ( $r_g$ )	$M_{\text{t0}}$ ( $M_\odot$ )	Neutrinos	Equatorial Outflow			Polar Outflow <sup>b</sup>			$M_{\text{pol}}$ ( $M_{\text{eq}}$ )	$M_{\text{ej,tot}}$ ( $M_{\text{t0}}$ )	$M_{\text{ej,unb}}$ ( $M_{\text{t0}}$ )
					$\bar{Y}_e$	$\bar{s}$ (k/b)	$t_{\text{exp}}$ (ms)	$\bar{Y}_e$	$\bar{s}$ (k/b)	$t_{\text{exp}}$ (ms)			
t-a00	0.00	6.00	0.03	Leak	0.19	19	31	...	...	...	...	0.05	0.03
t-a40	0.40	4.61			0.21	21	37	...	...	...	...	0.09	0.06
t-a80	0.80	2.91			0.22	21	35	0.31	38	9.4	0.01	0.17	0.11
t-a95	0.95	1.94			0.24	21	42	0.32	51	10	0.03	0.28	0.21
s-a00	0.00	6.00	0.03	Thin	0.18	20	35	...	...	...	...	0.05	0.03
s-a40	0.40	4.61			0.20	21	38	...	...	...	...	0.10	0.07
s-a80	0.80	2.91			0.22	21	38	...	...	...	...	0.19	0.13
s-a95	0.95	1.94			0.24	22	34	0.32	56	11	0.02	0.30	0.22
t-a80-hr	0.80	2.91	0.03	Leak	0.22	22	31	0.31	45	10	0.02	0.19	0.12
t-a00-bnd	0.00	6.00			0.18	19	35	...	...	...	...	0.05	0.03
j-a80v2	0.80	2.91	0.30	Leak	0.23	15	95	0.38	53	17	0.02	0.09	0.06
j-a80v5			0.30		0.20	17	54	0.29	28	16	0.04	0.17	0.09
j-a80m1			0.10		0.24	17	59	...	...	...	...	0.12	0.08

This potential reproduces the positions of the ISCO and horizon of the Kerr metric, and yields steady-state, sub-Eddington, thin accretion disk models that differ 10%–20% from the exact general-relativistic solution as computed by Artemova et al. (1996). In the context of time-dependent NS merger remnant accretion disk models, this potential has been employed by Setiawan et al. (2004), Setiawan et al. (2006), and Just et al. (2014).

Artemova et al. (1996) provide an analytic expression for the gravitational acceleration

$$\mathbf{g}_A = -\nabla\Phi_A = -\frac{GM_{\text{bh}}}{r^{2-\beta}(r-r_{\text{H}})^\beta}\hat{r}, \quad (1)$$

where  $\Phi_A$  is the potential,  $G$  is the gravitational constant,  $M_{\text{bh}}$  is the BH mass,  $r_{\text{H}}$  is the horizon radius of the Kerr metric

$$r_{\text{H}} = \left[1 + \sqrt{1 - a^2}\right] r_g, \quad (2)$$

with  $a$  the BH spin parameter,  $r_g = GM_{\text{bh}}/c^2$ , and  $\beta$  relates the horizon radius to the ISCO radius

$$\beta = \frac{r_{\text{ISCO}}}{r_{\text{H}}} - 1. \quad (3)$$

We use the analytic expression for  $r_{\text{ISCO}}(M_{\text{bh}}, a)$  in the Kerr metric (e.g., Bardeen et al. 1972).

Equation (1) can be integrated analytically, subject to the boundary condition  $\Phi_A \rightarrow 0$  for  $r \rightarrow \infty$ , yielding

$$\Phi_A(r) = \begin{cases} \frac{GM_{\text{bh}}}{(\beta-1)r_{\text{H}}} \left[ 1 - \left( \frac{r}{r-r_{\text{H}}} \right)^{\beta-1} \right] & (\beta \neq 1) \\ \frac{GM_{\text{bh}}}{r_{\text{H}}} \ln \left( 1 - \frac{r_{\text{H}}}{r} \right) & (\beta = 1) \end{cases} \quad (4)$$

for  $r > r_{\text{H}}$ . This expression reduces to the potential of

Paczynski & Wiita (1980) when  $a = 0$  ( $\beta = 2$ ). The case  $\beta = 1$  is obtained for a spin parameter  $a \simeq 0.68654$ . The expression for  $\beta \neq 1$  behaves well even for a spin parameter within  $10^{-5}$  of this critical value: the transition is continuous in  $\beta$ . For  $r \gg r_{\text{H}}$ , the potential asymptotes to the Newtonian expression.

One can use equation (4) to construct equilibrium tori for initial conditions using an arbitrary equation of state (FM13). When keeping all other parameters constant, an increase in BH spin increases the entropy of the torus at fixed distortion parameter (see, e.g., FM13 for a definition of the torus distortion parameter  $d$ ). Imposing a fixed entropy leads to changes of  $\sim 10\%$  in the distortion parameter when going from no-spin to near maximal spin. All other changes in the torus are minor.

While improved potential models exist relative to that of Paczynski & Wiita (1980) for non-spinning BHs (e.g., Tejeda & Rosswog 2013), to our knowledge no such improvements have been developed for the spinning case.

## 2.3 Models Evolved

We evolve two sequences of models with the spin rate of the BH as the only free parameter, as shown in Table 1. The baseline parameter set corresponds to the fiducial models S-def of FM13 and t000A3 (prompt BH) of Metzger & Fernández (2014): a BH mass  $M_{\text{bh}} = 3M_\odot$ , an initial disk mass  $M_{\text{t0}} = 0.03M_\odot$  with density peak located at a radial position  $R_0 = 50$  km, uniform electron fraction and entropy  $Y_e = 0.1$  and  $s = 8k_{\text{B}}/\text{baryon}$ , respectively, and a Shakura & Sunyaev (1973) parameter  $\alpha = 0.03$ . The ambient medium is set to have a density of  $\sim 1.1$  g/cm<sup>3</sup>.

The two sequences probe the same spin rates:  $a = \{0, 0.4, 0.8, 0.95\}$ , which sample a factor of 3 in ISCO radii,

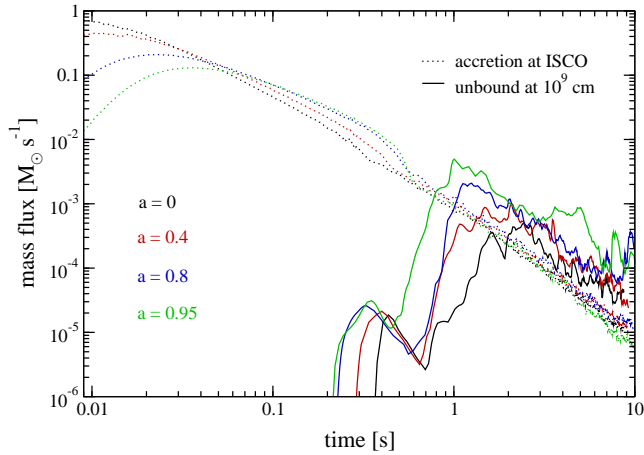


**Figure 1.** Mass outflow rate in unbound material at  $r \simeq 10^9$  cm (solid lines) and mass accretion rate at the ISCO (dotted lines) for models of the leakage sequence (t-series) with different BH spin.

as shown in Table 1. The sequences differ in the treatment of neutrinos, in order to assess the quantitative dispersion in the ejecta abundance and composition due to weak processes. The first sequence (t-models) makes use of the leakage scheme described in Metzger & Fernández (2014), while the second (s-models) uses the semi-transparent approach of FM13.

In addition, we evolve two models intended to test the consistency of our results. The first model repeats t-a80 at double resolution in radius and angle, to quantify the degree of convergence of integrated wind properties. The second model (t-a00-bnd) repeats the leakage model with no spin (t-a00,  $r_{\text{in}} = 4r_g$ ) but with an inner radial boundary located at the same position as the model with  $a = 0.8$  (t-a80,  $r_{\text{in}} = 2.25r_g$ ), to rule out boundary effects.

Finally, we evolve two models that mirror parameter choices made in Just et al. (2014), for comparison. Models j-a80v2 and j-a80v5 consist of a torus with mass  $M_{t0} = 0.3M_\odot$ , viscosity parameters  $\alpha = 0.02$  and  $0.05$ , respectively, and spin parameter  $a = 0.8$ . This combination corresponds to models M3A8m3a2-v2 and M3A3m3a5-v2 of Just et al. (2014), which implement the same type of shear-stress tensor. The initial entropy of these tori is chosen to be  $6k_B$  per baryon, so that the distortion parameter is comparable to the other models ( $d \simeq 2$ ) when going to high mass. A third model (j-a80m1) with torus mass  $M_{t0} = 0.1M_\odot$  and  $\alpha = 0.02$  is evolved to bridge the gap between these tori masses and the rest of our models.

### 3 RESULTS

Remnant accretion disks evolve in a generic way (Popham et al. 1999; Narayan et al. 2001; Chen & Beloborodov 2007). Initially, neutrino interactions are important. Depending on the mass of the disk and hence its optical depth, cooling of the disk can be delayed until the density becomes low enough for transparency (Kohri & Mineshige 2002; Di Matteo et al. 2002). As the disk evolves further, neutrino interactions shut down and the disk becomes radiatively-inefficient.

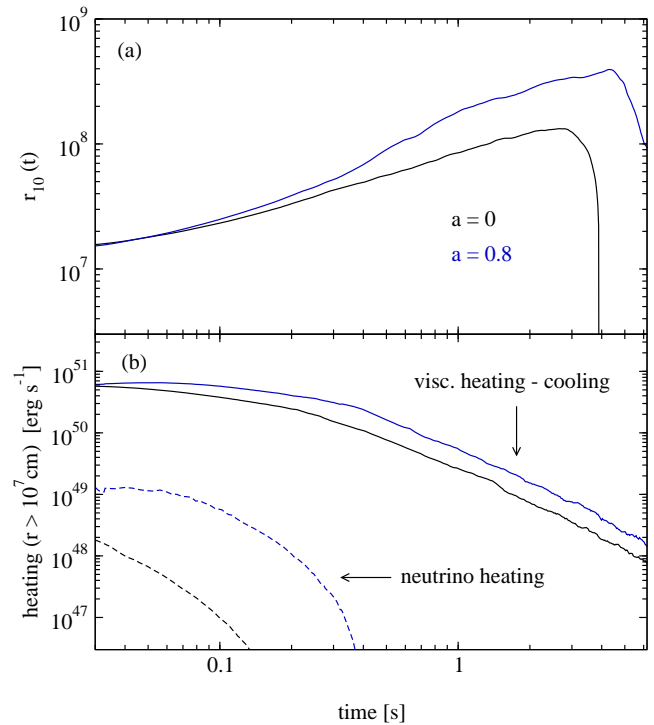


**Figure 2.** *Top:* Radius outside of which 10% of the initial disk mass ( $= 3 \times 10^{-3} M_\odot$ ) resides, as a function of time, for models t-a00 (black) and t-a80 (blue). The drop at late times occurs when the total mass remaining in the computational domain approaches the target value. *Bottom:* Integrated heating rate outside  $r = 10^7$  cm as a function of time for the same set of models. Solid lines show viscous heating minus net neutrino cooling  $[=\min(0, Q_\nu)]$ , with  $Q_\nu$  the net specific neutrino energy source term, and dashed lines show net neutrino heating  $[=\max(0, Q_\nu)]$ .

The bulk of mass ejection occurs after weak interactions freeze out on a timescale of  $\sim 1$  s (Metzger et al. 2008, 2009). At this time, viscous heating and nuclear recombination inject energy into the disk, without being offset by neutrino cooling. Because weak freezeout occurs from the outside in, this outflow is driven from the outermost parts of the disk, which have not been brought to beta equilibrium and hence have low electron fraction. Part of the outflow can be driven from the inner disk at earlier times, if neutrino self-irradiation can deposit enough energy to drive a thermal wind.

#### 3.1 Effect of BH spin on mass ejection

Mass ejection increases monotonically with spin, as shown in Table 1. In going from  $a = 0$  to  $a = 0.95$ , the amount of mass ejected increases by a factor larger than 5. Table 1 also shows that the ratio of unbound<sup>1</sup> to bound ejecta increases slightly ( $\sim 2$  to  $3$ ) with spin.

The outflow peaks earlier for models with larger spin, as measured<sup>2</sup> at a radius  $\simeq 10^9$  cm from the BH (Figure 1).

<sup>1</sup> We define unbound material as having positive total energy, including kinetic, internal, and gravitational contributions.

<sup>2</sup> For models with  $a = 0.95$ , the computational domain ends at  $r = 7.3 \times 10^8$  cm. The wind properties as a function of time are

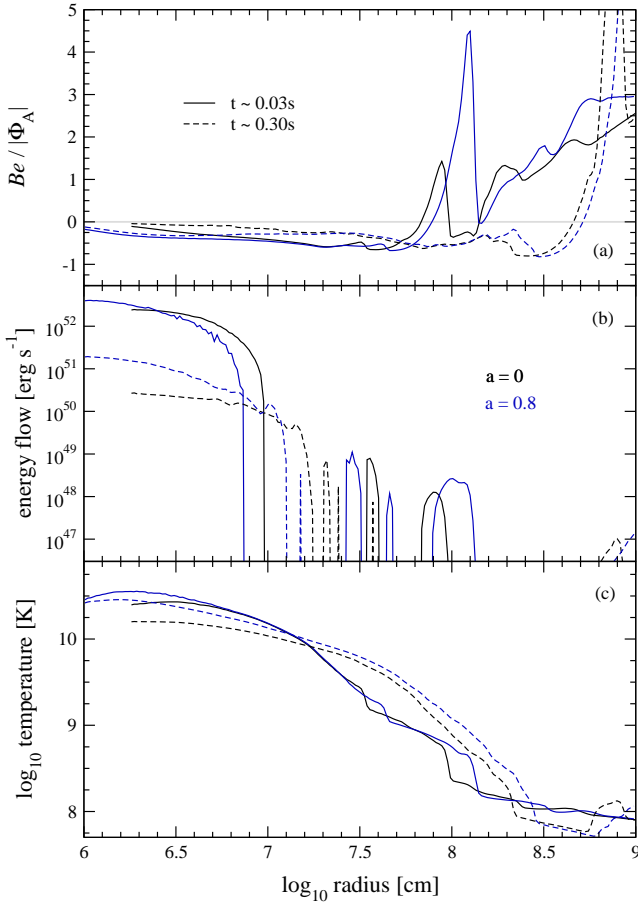


**Figure 3.** Radial profiles at two instants in the evolution of models t-a00 and t-a80, as labeled. Shown are (a) the angle-averaged, density-weighted Bernoulli parameter (eq. 5); (b) the surface-integrated energy flux as a function of radius (eq. 6); and (c) the angle-averaged, density-weighted temperature. The times correspond to a phase where neutrino cooling is important (0.03 s) and one in which the disk is becoming radiatively inefficient (0.3 s). Compare with Figure 2.

At any given time after models have settled into steady accretion, the mass accretion rate through the ISCO (which is spin-dependent) is lower for models with higher spin. This is consistent with existing studies of radiatively-inefficient accretion disks (Sądowski et al. 2013).

To illustrate the differences in evolution introduced by a higher BH spin, Figure 2 shows the radius outside of which 10% of the disk mass resides,  $r_{10}$ , as a function of time for models t-a00 and t-a80. Initially, this surface evolves similarly in both models until  $\sim 0.1$  s. Afterward, mass motion accelerates for the model with a spinning BH, settling later to a similar rate of expansion after  $\sim 1$  s. Figure 2 also shows the net heating rate outside  $10^7$  cm as a function of time. This heating rate is higher at all times for the model with  $a = 0.8$  after  $\sim 30$  ms of evolution. The enhancement is approximately a factor of  $\sim 2$ .

recorded close to this boundary and the resulting flow is injected into a larger computational domain in order to measure wind properties again at  $r = 10^9$  cm. Energy source terms are unimportant at these radii, and are thus neglected in this procedure.

This higher viscous energy deposition originates in the larger amount of energy released by the accretion flow when the inner edge of the accretion disk lies deeper in the potential well. Figure 3 shows radial profiles at two instants in the evolution of models t-a00 and t-a80. Shown is the angle-averaged, density-weighted Bernoulli parameter

$$Be = \frac{1}{2} \mathbf{v}^2 + e_{\text{int}} + \frac{p}{\rho} + \Phi_A, \quad (5)$$

normalized to  $|\Phi_A|$ , where  $\mathbf{v}$  is the total velocity including orbital motion,  $e_{\text{int}}$  is the specific internal energy including nuclear binding energy but normalized so that it vanishes at zero temperature,  $p$  is the pressure, and  $\rho$  is the density, as well as the surface-integrated energy flux,

$$\text{energy flow} \equiv 2\pi \int \sin \theta d\theta r^2 \rho v_r Be, \quad (6)$$

where the angular integral extends out to  $45^\circ$  from the mid-plane. The Bernoulli parameter of the accretion flow is negative in most of the disk. When accreting ( $v_r < 0$ ), energy thus flows outward. At early times, when the evolution of both models is very similar and neutrino cooling is important, the non-spinning BH releases slightly more energy at fixed radius. When the disk starts becoming radiatively-inefficient at  $\sim 0.3$  s, however, the energy flux in the spinning BH case is larger at all radii  $r < 10^7$  cm. At this time the disk with  $a = 0$  case satisfies  $|Be| \ll |\Phi_A|$  at small radii, while the spinning BH case is more gravitationally bound at fixed radius for  $r < 10^7$  cm.

The larger energy released in the spinning BH case results in a higher disk temperature at later times, as shown in Figure 3c. The higher temperature increases the rate of viscous heating, given that the kinematic viscosity coefficient in the parameterization of Shakura & Sunyaev (1973) is proportional to the sound speed squared, with the remaining factors that enter the heating rate depending only on gradients of the angular momentum or on position.

A higher temperature also results in more neutrino emission, which could in principle compensate for a higher viscous heating rate. However, neutrino cooling becomes unimportant for temperatures  $T < 1$  MeV (e.g., Metzger et al. 2009). Figure 3 shows that this corresponds approximately to the radius where the temperature profile changes slope around  $\sim 300$  km.

The global contribution from neutrino heating is minor in comparison to viscous heating. Figure 2b shows that the integrated neutrino heating rate at radii  $r > 10^7$  cm is only a few % of the net viscous heating rate. This is the case even in models with high spin, such as t-a80, in which there is a period of time from about 0.03 s to 0.3 s during which neutrino heating exceeds viscous heating in the radial range  $10^8 \text{ cm} < r < 3 \times 10^8 \text{ cm}$ . At these large radii the magnitude of the heating is quite small, however, and the contribution to the integrated heating rate is therefore small as well. In the non-spinning models, neutrino heating never exceeds viscous heating except in very localized spots at early times, with a negligible overall contribution.

Mass ejection in our models is essentially converged. Table 1 shows that doubling the resolution in radius and angle leads to an overall increase of only  $\sim 10\%$  in the outflow rate, as inferred by comparing models t-a80 and t-a80-hr. Changing the position of the inner boundary does not modify the mass ejection properties in any significant way, as

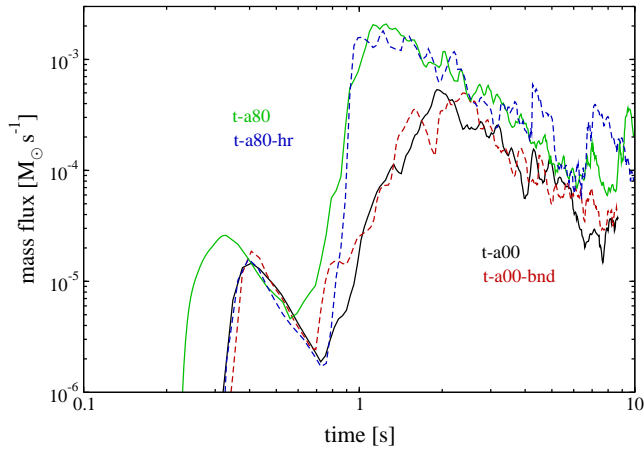


**Figure 4.** Mass outflow rate in unbound material at  $r = 10^9$  cm for different models that probe the robustness of our results. Models t-a00 (black-solid) and t-a00-bnd (red-dashed) differ only in the location of the inner radial boundary, with the latter having a minimum radius smaller by a factor 0.56. Model t-a80-hr (blue-dashed) has double resolution in radius and angle relative to model t-a80 (green-solid).

can be seen by comparing models t-a00 and t-a00-bnd, the latter using the inner boundary of a spinning BH model with  $a = 0.8$  ( $2.25r_g$  instead of  $4r_g$  for  $a = 0$ ). For comparison, the mass outflow rate at  $r = 10^9$  cm as a function of time is shown in Figure 4 for the four models (t-a00, t-a00-bnd, t-a80, t-a80-hr).

### 3.1.1 Comparison with previous work

Existing general relativistic, magnetohydrodynamic (MHD) simulations of radiatively-inefficient accretion disks find a correlation between the amount of mass ejected in the non-relativistic wind and the spin of the BH (Sądowski et al. 2013) that is qualitatively similar to what we find here. The character of this correlation also depends on the initial field geometry (McKinney et al. 2012). Direct comparison of our results with these studies can only be qualitative. On the one hand, the spatial distribution of heating in MHD is different than that obtained with an  $\alpha$  viscosity. In addition, the difference in initial conditions leads to very different evolutionary timescales, since these MHD studies are motivated by disks in AGN or X-ray binaries. Sądowski et al. (2013) do not find convergence on the mass ejection from the wind, because it is dominated by regions at large radii. The initial tori in these simulations extend from  $10r_g$  to  $1000r_g$  (Narayan et al. 2012), or have the initial density peak around  $100r_g$  (McKinney et al. 2012). Models are evolved for a maximum time of  $2 \times 10^5 r_g/c$ . In contrast, our initial tori have the density maximum at  $11r_g$ , and are evolved for  $\simeq 6.7 \times 10^5 r_g/c$ . A smaller radius implies that the disk can evolve on a shorter time.

Regarding our subset of models that mirror parameters from Just et al. (2014), we find overall agreement in mass ejection for the case of model j80-v5 at 17% of the initial disk mass. This is somewhat lower than model M3A8m3a5-v2 of Just et al. (2014), which ejects 23% of the initial disk mass, but still consistent given the  $\sim 10\%$  uncertainty introduced by resolution. In contrast, our model with lower viscosity

(j80-v2) ejects only 9% of the initial disk mass, whereas model M3A8m3a2-v2 of Just et al. (2014) ejects 21%. To ensure that this discrepant result is not a numerical artifact, we evolved a model with  $\alpha = 0.02$  and  $M_{t0} = 0.1M_\odot$ , intermediate between our fiducial model sequence and the disk masses of Just et al. (2014). The fraction of the disk mass ejected in this case is 12%, approximately midway between what is obtained for models t-a80 and t-a80-hr (17 – 19%) and model j80-v2. Therefore, we find a dependence of the ejecta mass on the disk mass, with more massive disks ejecting a lower fraction. Given that the only significant difference between our setup and that of Just et al. (2014) is the neutrino physics, we surmise that the discrepant ejecta masses come from stronger cooling in our leakage scheme at large tori masses.

### 3.2 Effect of BH spin on outflow composition

To characterize the bulk properties of the outflow, we take mass-flux-weighted averages as in FM13

$$\bar{A} = \frac{\int A(r_{\text{out}}, \theta) F_M(r_{\text{out}}, \theta) d\theta dt}{\int F_M(r_{\text{out}}, \theta) d\theta dt}, \quad (7)$$

where  $F_M = \rho v_r$ ,  $r_{\text{out}}$  is defined so that  $\bar{T} \simeq 5 \times 10^9$  K, the time integral is taken over the entire simulation, and the angular integral is restricted to equatorial ( $60^\circ$  from the equator) and polar ( $30^\circ$  from the axis) latitudes.

The mean electron fraction in the equatorial outflow increases very modestly though monotonically with spin, as shown in Table 1. For the neutrino leakage sequence,  $\bar{Y}_e$  increases from 0.19 to 0.24 when going from  $a = 0$  to  $a = 0.95$ . A similar change is obtained in the sequence with optically thin neutrino treatment.

The origin of this increase lies in a component of the wind that is more strongly irradiated by neutrinos than the rest of the wind, arising from regions above the disk midplane at small radius and at time  $t \sim 0.1$  s. Figure 5 illustrates how this component differs in models with and without spin (t-a00 and t-a80). In both cases, a radial outflow at intermediate latitudes is apparent. This outflow wraps around the back side of the disk, and mixes with the material in the outer disk midplane, given that the disk is convective at this time.

In the spinning BH case, this irradiated component has a significantly higher electron fraction than the rest of the disk, contributing to raise the mean  $Y_e$  of the equatorial outflow. Strong irradiation in a spinning BH results from the neutrino luminosities remaining high for a longer period of time, as shown in Figure 6. Once the neutrino luminosities decay around  $t \sim 0.3$  s, this outflow ceases to contribute high- $Y_e$  material. As pointed out in §3.1, neutrino heating never exceeds viscous heating in the inner disk, hence we refer to this component as *neutrino-irradiated* instead of *neutrino-driven*.

The entropy and expansion time at  $r_{\text{out}}$  in the equatorial outflow also undergo moderate to insignificant changes with increasing BH spin, reflecting the dominance of viscous energy deposition in setting the outflow properties. Further support for this hypothesis comes from the fact that overall results in the leakage and optically thin sequences are very similar, despite non-negligible differences in neutrino



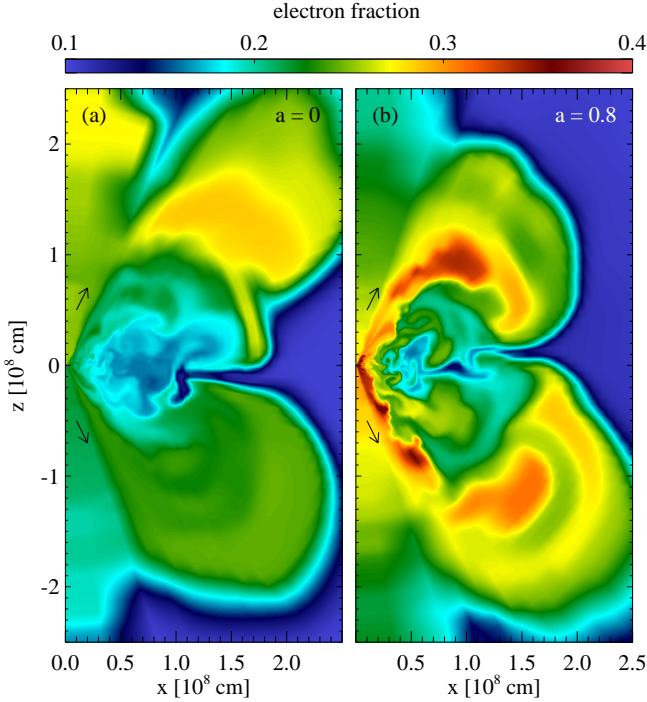


**Figure 5.** Electron fraction in models t-a00 (left) and t-a80 (right) at times 0.78 s and 0.45 s, respectively, when their winds have reached a similar level of expansion. The arrows indicate the direction in which neutrino-irradiated material moves.

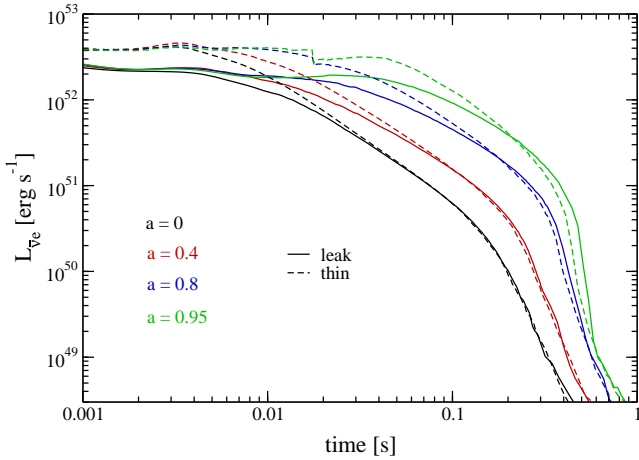


**Figure 6.** Electron antineutrino luminosity for models with different spin parameter and neutrino treatment. Shown are models in the sequence with neutrino leakage (t-sequence, solid) and optically thin emission with corrections (s-sequence, dashed). Colors correspond to different BH spin parameters, as shown.

emission properties (e.g., the magnitude of the neutrino luminosities in Figure 6).

The signature of a neutrino-driven wind is the ejection of material along the polar direction. When the BH has no spin, we cannot find a value of  $r_{\text{out}}$  where  $\bar{T} = 5 \times 10^9$  for polar latitudes (at this temperature heavy elements begin to form). This failure to find an outflow is due to the polar cavity being mostly devoid of material. Increasing the BH spin

**Table 2.** Ejected mass for models in the leakage and optically-thin sequences, measured at  $10^9$  cm and after  $\sim 10$  s. Columns show from left to right model name, total ejected mass, ejected mass with  $Y_e \geq 0.25$ , and ejected mass with  $Y_e \geq 0.3$ , respectively. See Table 1 for model parameters.

Model	$M_{\text{ej,tot}}$ ( $\times 10^{-3} M_{\odot}$ )	$M_{\text{ej}, Y_e \geq 0.25}$ ( $M_{\odot}$ )	$M_{\text{ej}, Y_e \geq 0.3}$ ( $M_{\odot}$ )
t-a00	1.5	$9.8 \times 10^{-6}$	$6.7 \times 10^{-7}$
t-a40	2.8	$2.0 \times 10^{-4}$	$6.8 \times 10^{-7}$
t-a80	5.1	$9.9 \times 10^{-4}$	$7.3 \times 10^{-5}$
t-a95	8.4	$3.0 \times 10^{-3}$	$9.3 \times 10^{-4}$
s-a00	1.6	$1.1 \times 10^{-5}$	$5.7 \times 10^{-7}$
s-a40	3.0	$2.3 \times 10^{-4}$	$6.9 \times 10^{-7}$
s-a80	5.8	$7.4 \times 10^{-4}$	$1.5 \times 10^{-6}$
s-a95	9.0	$3.0 \times 10^{-3}$	$5.8 \times 10^{-4}$

results in more material being ejected from the inner disk into polar latitudes. To estimate this fraction of the outflow, we compute the total mass ejected at  $r_{\text{out}}$  toward polar latitudes, whenever this quantity is well-defined, and compare it with the total mass ejected on equatorial latitudes at the same radius. The result is shown in Table 1. In all cases, the fraction of the mass ejected towards polar latitudes is a few percent of the total outflow. The composition of this polar outflow is noticeably different, however. The electron fractions are  $Y_e > 0.3$  in all cases, with entropies a factor of  $\sim 2$  higher and expansion times a factor  $\sim 3$  shorter than the equatorial outflow.

The full range of nucleosynthetic- and EM transient-relevant properties in the outflow is shown in Figure 7, which displays mass histograms of electron fraction, entropy, expansion time, and asymptotic velocity for all models in the leakage sequence. The first three histograms from the left are constructed using mass ejected at all angles at  $r_{\text{out}}$ , and include material that moves outward and inward, yielding a normalization that matches<sup>3</sup> the total mass ejected at  $r_{\text{out}}$ . The overall shape of the histograms matches the trend in the mass-flux-weighted quantities shown in Table 1. Very similar results are found for the optically-thin sequence.

The asymptotic velocity histogram (rightmost) shows only unbound material, and the mass ejected is computed at  $r = 10^9$  cm (c.f. Figure 1). The wind is sub-relativistic, with asymptotic velocities  $\sim 0.05c$ . The mean velocity increases only moderately (though still monotonically) with BH spin.

The fraction of the outflow with Lanthanide-free composition is of particular interest to the observed kilonova properties. Due to the lower opacities, this material should produce a bluer, optical ‘bump’ in the otherwise infrared kilonova, facilitating its detection at early times. For the mean entropies and expansion times of these winds, the transition between Lanthanide-free and Lanthanide-rich is quite abrupt, and occurs in the range  $Y_e = 0.25 - 0.3$  (Kasen et al. 2014, in preparation). We have computed the fraction of the total ejecta mass with  $Y_e \geq 0.25$  and  $Y_e \geq 0.3$ . Results are shown in Table 2. For the most likely spin rate ( $a = 0.8$ ),

<sup>3</sup> FM13 only included material that moves outward.

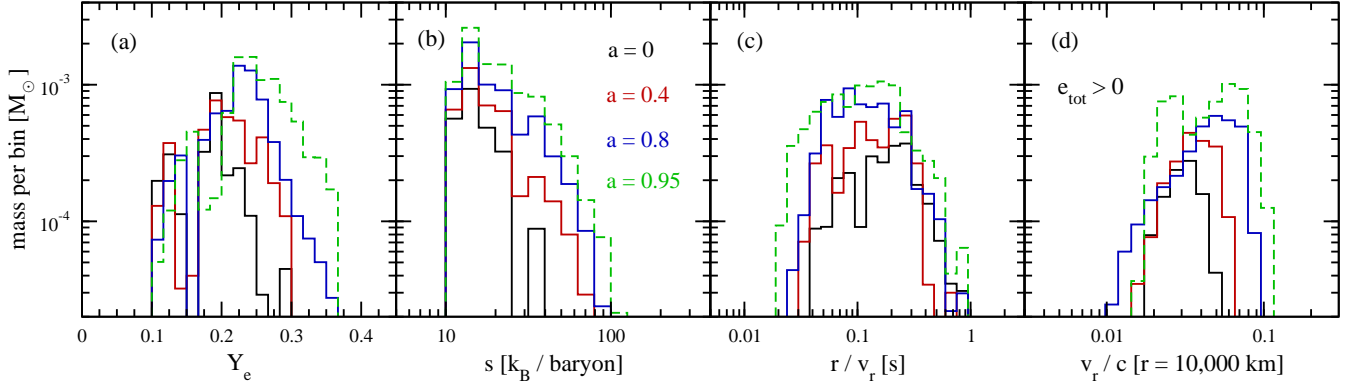


**Figure 7.** Mass histograms of quantities relevant for nucleosynthesis and EM transients, for models of the t-sequence (see Table 1 for model parameters). The first three panels from the left show mass distributions as a function of electron fraction, entropy, and expansion time. These histograms are generated at a radius such that the mass-flux-weighted temperature is  $\sim 5 \times 10^9$  K, and including bound and unbound material. The rightmost panel shows mass distribution as function of the velocity of the *unbound* material only, computed at  $r = 10^9$  cm.

the fraction of the ejecta that would contribute to a ‘blue’ precursor ranges from 1 – 10% of the outflow.

The location of the Lanthanide-free ejecta is also important, as it must be exterior to the high-opacity, low- $Y_e$  material, otherwise any optical emission will be obscured. Figure 8 shows the spatial distribution of the electron fraction for model t-a80 at time 300 s, when the velocity distribution is very close to homologous. We obtain this distribution by recording the properties of the wind at a radius  $10^9$  cm as a function of time. At this position, neutrino and viscous source terms operate slowly relative to the expansion time. The sampled wind is then injected into a much larger computational domain with lower ambient density, without energy source terms, allowing it to expand freely for times much longer than 10 s. A more complete description of this procedure will be presented in Kasen et al. (2014, in preparation). The homologous ejecta is approximately spherical, and because the higher  $Y_e$  material is ejected at earlier times in the neutrino-irradiated outflow that wraps around the disk (Figure 5), it precedes the more neutron-rich component. This Lanthanide-free ‘skin’ of material would likely give rise to a blue ‘bump’ in the kilonova light curve, occurring on timescales of  $\lesssim 1$  day and with optical luminosities of the order of  $10^{40} - 10^{41}$  erg s $^{-1}$ .

#### 4 SUMMARY AND DISCUSSION

In this paper we have systematically examined the effect of BH spin on the properties of winds from NS-NS and NS-BH merger remnant accretion disks. We have used two-dimensional, time-dependent hydrodynamic simulations of the viscous evolution of these disks, modeling the spacetime of a rotating BH via a pseudo-Newtonian potential, and using two different approximations to the neutrino physics. Our main results are the following:

1. – Increasing the spin of the BH increases the amount of mass ejected due to weak freezout of the disk (Figure 1). This enhancement can be a factor of  $\sim 5$  for  $a = 0.95$  relative to the non-spinning case (Table 1). The ratio of

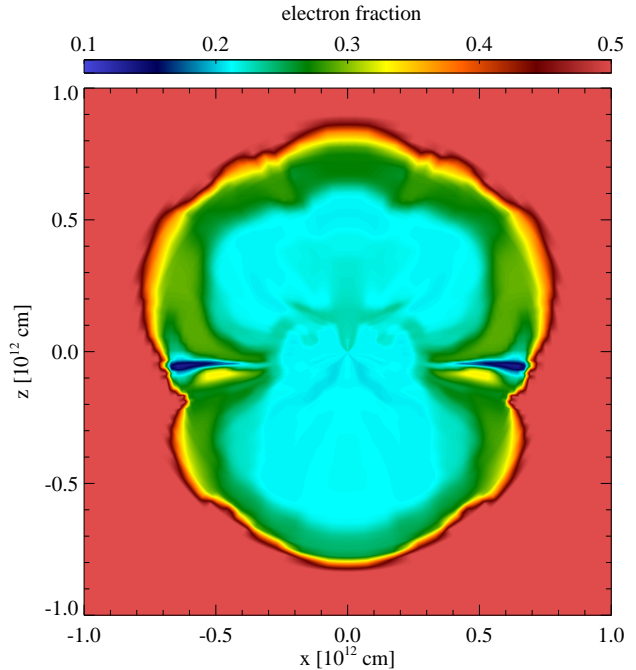


**Figure 8.** Electron fraction for model t-a80-hr at time  $t = 300$  s, when most of the ejecta mass has reached homologous expansion. Material with  $Y_e \simeq 0.3$  and hence low optical opacity is ahead of more neutron-rich ejecta, with the potential for the generation of a ‘blue’ bump in the infrared kilonova. The ambient medium has electron fraction  $Y_e = 1$  (pure hydrogen, beyond the limits of the color table).

unbound to bound ejecta also increases with increasing spin.

2. – The increase mass ejection at higher spin stems from higher net energy deposition by viscous heating (Figure 2). The larger heating is related to a higher energy released by the accretion flow given the smaller ISCO of a spinning BH (Figure 3). Neutrino heating makes a minor contribution to the global energy deposition. This is the main reason why our two different neutrino implementations lead to



very similar results, despite noticeable differences in the neutrino luminosities (Figure 6).

3. – The mean electron fraction of the outflow increases monotonically with increasing spin, all else being equal (Table 1). However, the magnitude of this increase is moderate. For our fiducial parameter choice, increasing the spin from 0 to 0.95 increases the mean electron fraction from  $\sim 0.19$  to  $\sim 0.24$ . The bulk of the outflow is still very neutron-rich.

4. – The increase in electron fraction stems primarily from mixing of the equatorial outflow with a distinctive, neutrino-irradiated component. This component originates in regions at high altitude above the midplane and small cylindrical radius (Figure 5). The primary driver of this outflow is not neutrino heating, though its composition is strongly affected by neutrino irradiation.

5. – Other outflow properties such as the mean entropy, expansion time, and asymptotic velocity are not very sensitive to the spin of the BH (Figure 7).

6. – For the most likely spin value ( $a = 0.8$ ), the fraction of the ejecta that has Lanthanide-free composition ranges from 1 to 10% (Table 2). This high- $Y_e$  material resides at the leading edge of the wind (Figure 8), with the potential to generate an early ( $\lesssim 1$  day) ‘blue bump’ in the infrared kilonova.

Our results are in general agreement with the closely related work of Just et al. (2014). At spins comparable with those in their models ( $a = 0.8$ ), we obtain total outflow rates  $\sim 20\%$ , mean electron fractions close to  $\sim 0.25$ , and entropies  $\sim 20$   $k_B$  per baryon. While we identify a distinctive component of the outflow that is strongly irradiated by neutrinos, we do not find any dynamically important region where neutrino heating dominates over viscous heating. Our main difference with Just et al. (2014) is quantitative, and concerns the fraction of the ejecta mass with  $Y_e$  significantly higher than 0.3. We attribute this discrepancy to the difference in neutrino implementation. Given that their treatment of neutrino emission and self-irradiation is more sophisticated than ours, our models are likely underestimating the fraction of the material that generates Lanthanide-free ejecta.

While the wind from a spinning BH can in principle generate a blue precursor to an  $r$ -process kilonova, there are qualitative differences between this outflow and that from a long-lived HMNS (Metzger & Fernández 2014). First, the total amount of ejecta is smaller by a factor of several in the BH case. Out of this material, only a small fraction satisfies the Lanthanide-free conditions. Second, the geometry of the wind from a spinning BH is still mostly spherical, while the outflow from a HMNS has a  $\sim 2 : 1$  asymmetry (Kasen et al. 2014, in preparation). Therefore a long delay to BH formation should lead to a stronger geometric dependence and higher intensity of the ‘blue’ precursor.

If the most likely spin of a BH remnant is  $a = 0.8$ , then a fraction  $\sim 20\%$  of the initial disk mass is ejected. Galactic chemical evolution models require an ejected mass in  $r$ -process elements of  $\sim 0.01 M_\odot$  per

event to account for the abundance scatter in galactic halo stars (Tsujiimoto & Shigeyama 2014; Shen et al. 2014; van de Voort et al. 2014). If a prompt BH is the most likely outcome of a NS-NS or NS-BH merger, our results suggest that these events can produce sufficient amounts of  $r$ -process elements to explain the Galactic abundance, even if the merger rate is on the lower end of the expected value. The absolute mass of the disk and of the dynamical ejecta can vary due to a number of factors, and therefore the ratio of light to heavy  $r$ -process elements can in principle also vary from event to event, generating an intrinsic dispersion in the abundance pattern (Just et al. 2014).

An improved estimate for the amount of mass ejected in these winds and its composition will require the use of general relativistic (GR) models. The highest spins explored here ( $a = 0.95$ ) are such that the ISCO is already close to the horizon. Our pseudo-Newtonian treatment is thus pushed beyond its limit of validity for these extreme cases.

An equally important improvement concerns the inclusion of MHD. The spatial distribution of heating is different in a disk where MHD turbulence transports angular momentum relative to one where viscosity is employed (e.g., Hirose et al. 2006). This has implications for the location of the wind driving and its intensity. In addition, a disk around a spinning BH in MHD is expected to power a jet via the Blandford-Znajek mechanism (Blandford & Znajek 1977; see also Tchekhovskoy et al. 2011), with an energy output that can dominate over that in the non-relativistic wind (e.g., Sądowski et al. 2013). Such a jet is thought to be at the heart of the short gamma-ray burst central engine, and its inclusion in the evolution of the system would help to better predict the early phases of an electromagnetic transient.

Finally, a reliable prediction for the composition of the ejecta will require, in addition to GR and MHD, good neutrino transport. This is essential in order to quantify the electron fraction of the strongly-irradiated component of the wind (whether neutrino-driven or not), and the angle-dependent composition of the ejecta.

## ACKNOWLEDGMENTS

We thank Oliver Just, Thomas Janka, Albino Perego, Stephan Rosswog, Sasha Tchekhovskoy, and Francois Foucart for stimulating discussions and/or comments on the manuscript. We also thank the referee, Maximilian Ruffert, for constructive comments that improved the paper. RF acknowledges support from the University of California Office of the President, and from NSF grant AST-1206097. DK was supported in part by a Department of Energy Office of Nuclear Physics Early Career Award, and by the Director, Office of Energy Research, Office of High Energy and Nuclear Physics, Divisions of Nuclear Physics, of the U.S. Department of Energy under Contract No. DE-AC02-05CH11231. BDM acknowledges support from NSF grant AST-1410950 and the Alfred P. Sloan Foundation. EQ was supported by NSF grant AST-1206097, the David and Lucile Packard Foundation, and a Simons Investigator Award from the Simons Foundation. This work was supported in part by National Science Foundation Grant No. PHYS-1066293 and the hospitality of the Aspen Center for Physics. The

software used in this work was in part developed by the DOE NNSA-ASC OASCR Flash Center at the University of Chicago. This research used resources of the National Energy Research Scientific Computing Center (NERSC), which is supported by the Office of Science of the U.S. Department of Energy under Contract No. DE-AC02-05CH11231. Computations were performed at the *Carver* cluster.

## REFERENCES

- Abadie J., et al., 2010, *Classical and Quantum Gravity*, 27, 173001
- Artemova I. V., Bjoernsson G., Novikov I. D., 1996, *ApJ*, 461, 565
- Bardeen J. M., Press W. H., Teukolsky S. A., 1972, *ApJ*, 178, 347
- Barnes J., Kasen D., 2013, *ApJ*, 775, 18
- Bauswein A., Goriely S., Janka H.-T., 2013, *ApJ*, 773, 78
- Berger E., Fong W., Chornock R., 2013, *ApJ*, 774, L23
- Blandford R. D., Znajek R. L., 1977, *MNRAS*, 179, 433
- Bloom J. S., et al., 2009, *Astro 2010 Decadal Survey Whitepaper*, arXiv:0902.1527
- Chen W.-X., Beloborodov A. M., 2007, *ApJ*, 657, 383
- Dessart L., Ott C. D., Burrows A., Rosswog S., Livne E., 2009, *ApJ*, 690, 1681
- Di Matteo T., Perna R., Narayan R., 2002, *ApJ*, 579, 706
- Dubey A., Antypas K., Ganapathy M. K., Reid L. B., Riley K., Sheeler D., Siegel A., Weide K., 2009, *J. Par. Comp.*, 35, 512
- Fernández R., 2012, *ApJ*, 749, 142
- Fernández R., Metzger B. D., 2013a, *MNRAS*, 435, 502
- Fernández R., Metzger B. D., 2013b, *ApJ*, 763, 108
- Foucart F., Deaton M. B., Duez M. D., O'Connor E., Ott C. D., Haas R., Kidder L. E., Pfeiffer H. P., Scheel M. A., Szilagyi B., 2014, *PRD*, 90, 024026
- Freiburghaus C., Rosswog S., Thielemann F., 1999, *ApJ*, 525, L121
- Ghosh S., Nelemans G., 2014, arXiv:1406.0343
- Goriely S., Sida J.-L., Lemaître J.-F., Panebianco S., Dubray N., Hilaire S., Bauswein A., Janka H.-T., 2013, *Physical Review Letters*, 111, 242502
- Grossman D., Korobkin O., Rosswog S., Piran T., 2014, *MNRAS*, 439, 757
- Hirose S., Krolik J. H., Stone J. M., 2006, *ApJ*, 640, 901
- Hotokozaka K., Kiuchi K., Kyutoku K., Okawa H., Sekiguchi Y.-i., Shibata M., Taniguchi K., 2013, *Phys. Rev. D*, 87, 024001
- Just O., Bauswein A., Ardevol Pulpillo R., Goriely S., Janka H.-T., 2014, *MNRAS*, submitted, arXiv:1406.2687
- Kasen D., Badnell N. R., Barnes J., 2013, *ApJ*, 774, 25
- Kasliwal M. M., Nissanke S., 2014, *ApJ*, 789, L5
- Kiuchi K., Sekiguchi Y., Shibata M., Taniguchi K., 2009, *Phys. Rev. D*, 80, 064037
- Kohri K., Mineshige S., 2002, *ApJ*, 577, 311
- Korobkin O., Rosswog S., Arcones A., Winteler C., 2012, *MNRAS*, 426, 1940
- Lattimer J. M., Schramm D. N., 1974, *ApJ*, 192, L145
- Lee W. H., Ramirez-Ruiz E., López-Cámara D., 2009, *ApJ*, 699, L93
- Li L., Paczyński B., 1998, *ApJ*, 507, L59
- McKinney J. C., Tchekhovskoy A., Blandford R. D., 2012, *MNRAS*, 423, 3083
- McLaughlin G. C., Surman R., 2005, *Nuclear Physics A*, 758, 189
- Metzger B. D., Berger E., 2012, *ApJ*, 746, 48
- Metzger B. D., Fernández R., 2014, *MNRAS*, 441, 3444
- Metzger B. D., Martínez-Pinedo G., Darbha S., Quataert E., Arcones A., Kasen D., Thomas R., Nugent P., Panov I. V., Zinner N. T., 2010, *MNRAS*, 406, 2650
- Metzger B. D., Piro A. L., Quataert E., 2008, *MNRAS*, 390, 781
- Metzger B. D., Piro A. L., Quataert E., 2009, *MNRAS*, 396, 304
- Narayan R., Piran T., Kumar P., 2001, *ApJ*, 557, 949
- Narayan R., Sądowski A., Penna R. F., Kulkarni A. K., 2012, *MNRAS*, 426, 3241
- Nissanke S., Kasliwal M., Georgieva A., 2013, *ApJ*, 767, 124
- Oechslin R., Janka H.-T., Marek A., 2007, *A&A*, 467, 395
- Paczynski B., Wiita P. J., 1980, *A&A*, 88, 23
- Perego A., Rosswog S., Cabezón R. M., Korobkin O., Käppeli R., Arcones A., Liebendörfer M., 2014, *MNRAS*, 443, 3134
- Popham R., Woosley S. E., Fryer C., 1999, *ApJ*, 518, 356
- Rezzolla L., Baiotti L., Giacomazzo B., Link D., Font J. A., 2010, *Classical and Quantum Gravity*, 27, 114105
- Roberts L. F., Kasen D., Lee W. H., Ramirez-Ruiz E., 2011, *ApJ*, 736, L21
- Ruffert M., Janka H.-T., Takahashi K., Schaefer G., 1997, *A&A*, 319, 122
- Sądowski A., Narayan R., Penna R., Zhu Y., 2013, *MNRAS*, 436, 3856
- Setiawan S., Ruffert M., Janka H.-T., 2004, *MNRAS*, 352, 753
- Setiawan S., Ruffert M., Janka H.-T., 2006, *A&A*, 458, 553
- Shakura N. I., Sunyaev R. A., 1973, *A&A*, 24, 337
- Shen S., Cooke R., Ramirez-Ruiz E., Madau P., Mayer L., Guedes J., 2014, *ApJL*, submitted, arXiv:1407.3796
- Singer L. P., Price L. R., Farr B., Urban A. L., Pankow C., Vitale S., Veitch J., Farr W. M., Hanna C., Cannon K., Downes T., Graff P., Haster C.-J., Mandel I., Sidery T., Vecchio A., 2014, *ApJ*, submitted, arXiv:1404.5623
- Surman R., McLaughlin G. C., Hix W. R., 2006, *ApJ*, 643, 1057
- Surman R., McLaughlin G. C., Ruffert M., Janka H.-T., Hix W. R., 2008, *ApJ*, 679, L117
- Tanaka M., Hotokezaka K., 2013, *ApJ*, 775, 113
- Tanvir N. R., Levan A. J., Fruchter A. S., Hjorth J., Hounsell R. A., Wiersema K., Tunnicliffe R. L., 2013, *Nature*, 500, 547
- Tchekhovskoy A., Narayan R., McKinney J. C., 2011, *MNRAS*, 418, L79
- Tejeda E., Rosswog S., 2013, *MNRAS*, 433, 1930
- Timmes F. X., Swesty F. D., 2000, *ApJS*, 126, 501
- Tsujiimoto T., Shigeyama T., 2014, *A&A*, 565, L5
- van de Voort F., Quataert E., Hopkins P. F., Keres D., Faucher-Giguere C.-A., 2014, *MNRAS*, submitted, arXiv:1407.7039
- Wanajo S., Janka H.-T., 2012, *ApJ*, 746, 180